

# Statistical Mechanics and Molecular Simulation of Adsorption in Microporous Materials: Pillared Clays and Carbon Molecular Sieve Membranes<sup>†</sup>

Jaleh Ghassemzadeh, Lifang Xu, Theodore T. Tsotsis, and Muhammad Sahimi\*

Department of Chemical Engineering, University of Southern California, Los Angeles, California 90089-1211

Received: October 8, 1999

We report the results of extensive equilibrium molecular dynamics simulation of adsorption of single-component and binary gas mixtures in models of two classes of microporous materials, namely, pillared clays and carbon molecular sieve membranes (CMSMs), both of which have been utilized for separation of gas mixtures. We develop a novel three-dimensional molecular pore network model for CMSMs based on Voronoi tessellation. The simulations allow us to investigate the effect of the morphology of the pore space, i.e., its pore size distribution and pore connectivity on the adsorption isotherms. The simulation results are also used to test the accuracy of a recently developed statistical mechanical theory of adsorption. The theory is shown to provide very accurate predictions for the simulation results for both classes of the microporous materials over a wide range of the porosity of the porous materials.

## Introduction

Porous materials have been used for separation of gas mixtures into their components by means of adsorption on the pores' walls and molecular sieving. Transport and sorption processes in such porous materials are currently subjects of considerable research activity. In practical applications these phenomena involve large molecules with sizes that are comparable to those of the pores. In the chemical, environmental, and gas purification industries, for example, adsorptive separation has gained ever increasing utilization since the successful discovery of zeolites, activated carbon, and carbon molecular sieve membranes (CMSMs) and adsorbents.<sup>1–3</sup> In general, adsorptive separation processes can be classified into three groups. The first group involves equilibrium separation in which, in analogy with distillation and extraction, separation is achieved by virtue of differences between the distribution of individual components in the adsorbent and fluid phases. In the second group is steric separation, which is associated with exclusion of some of the molecules from entering the pore structure owing to their different shapes and sizes, while the third involves kinetic separation caused by virtue of the differences in the diffusion rates of adsorbate molecules into the adsorbent materials. Among these, equilibrium separation is, by far, the most commonly used adsorptive separation method in industrial applications. As a result, understanding adsorption equilibria of gas mixtures in microporous materials is of great importance in process design and optimization of separation processes. Theories of multicomponent adsorption based on classical thermodynamics and statistical mechanics have been developed<sup>4,5</sup> and have attracted wide attention. Though they have proven quite successful in correlating experimental results at low pressures, several studies indicate that at high pressures (or equivalently, at high loading conditions) there are significant deviations between the predictions of such theories and the experimental data. The deviations increase sharply with pressure.

In this paper we study adsorption equilibria of gas mixtures in model microporous media. In particular, we are interested in

the adsorption of gas mixtures in microporous materials that have interconnected pores. Although such materials are used routinely in practical applications, previous studies have been restricted mostly to investigating these phenomena in a single pore, whereas the morphology of the pore space is one of the most important controlling factors in separation of fluids in a porous medium.<sup>6,7</sup> One of the main goals of our study is to understand the effect of the structure of the pore space on adsorption of gas mixtures. To investigate this issue, we construct molecular models for two classes of microporous materials that are currently of great practical interest, namely, pillared clays (PCs) and CMSMs. These two classes of microporous materials have completely different morphologies. Thus, they can provide a testing ground for theories of adsorption in microporous media and describing the effect of their pore space structure on the adsorption process. They have both been used for separation of gas mixtures into their constituents.

Pillared clays were originally developed as a new class of catalytic materials. Among such materials zeolites have received the widest attention. However, in recent years a number of investigators have studied adsorption in PCs. Most of these studies are experimental in nature;<sup>8–20</sup> for a review, see Klopogge.<sup>21</sup> The synthesis of PCs was originally suggested by Barrer and McLeod.<sup>22</sup> They inserted molecules into clay minerals to prop apart the aluminosilicate sheets, thereby producing larger pores than those commonly found in native clays, or even in zeolites. However, the resulting porous materials did not have the thermal stability that zeolites usually possess. Pillars of hydroxyaluminum and other cations are capable of being dehydrated to oxide pillars and withstand temperatures of up to 500 °C without structural collapse under catalytic cracking conditions. They are relatively new and were first reported by Brindley and co-workers<sup>23,24</sup> and independently by Lahav et al.<sup>25</sup> and Vaughan and Lussier.<sup>26</sup> In general, pillared montmorillonites are 2:1 dioctahedral clay minerals consisting of layers of silica in tetrahedral coordination, holding between them a layer of alumina in octahedral coordination. Substituting Si<sup>4+</sup> with Al<sup>3+</sup>, or Al<sup>3+</sup> with Mg<sup>2+</sup>, gives the silicate layer a

<sup>†</sup> Part of the special issue "Harvey Scher Festschrift".

\* Corresponding author. Electronic mail: moe@iran.usc.edu.

negative net charge, which is normally compensated by  $\text{Na}^+$ ,  $\text{Ca}^{2+}$ , and  $\text{Mg}^{2+}$  ions.<sup>27</sup> By exchanging the charge-compensating cations with large cationic oxyaluminum polymers, one can synthesize molecular-sieve-type materials.<sup>25,26</sup> Upon heating, these inorganic polymers form pillars that prop open the clay layer structure and form permanent PCs. The location and size of the pillars can, in general, vary, depending on such parameters as the type of the pillaring agent and the preparation conditions. Similar to zeolite-based catalysts, PCs have shown high catalytic activities for gas oil cracking, and large initial activities toward methanol conversion to olefins and toluene ethylation, but they are substantially deactivated by coke deposition.<sup>28</sup> For use in catalytic processes, PCs offer the advantage that their pore sizes can be made larger than those of faujastitic zeolites. They are also flexible enough to be used in separation processes,<sup>16–19,29</sup> because access to their interior pore volume can be controlled by the distance between the silicate layers and the distance between the pillars. One or both can be adjusted to suit a particular separation application. Despite their many potential applications and the existence of a wealth of experimental data, very few fundamental theoretical or computer simulation studies have been carried out so far to investigate adsorption (and transport) processes in PCs.<sup>30–34</sup> Molecular simulations of adsorption and diffusion in model PCs were initiated by our group.<sup>35–37</sup> Using grand-canonical-ensemble Monte Carlo and molecular dynamics (MD) simulations, we previously studied adsorption and diffusion of simple gas molecules in model PCs. In the present paper we extend our previous studies and use MD simulation to study adsorption of binary gas mixtures in PCs. Most of the previous molecular simulations of gas mixtures in porous media have been restricted to a single pore,<sup>38–47</sup> with the notable exception of Segarra and Glandt.<sup>48</sup>

Over the past few years, CMSMs, prepared by carbonization of polymeric precursors, have been studied as a promising alternative to both inorganic (such as  $\text{SiO}_2$  and metal membranes) and polymeric membranes.<sup>49–56</sup> Various precursors and preparation techniques have been used, a summary of which is given in two recent papers by our group.<sup>57,58</sup> Our group has prepared CMSMs using a polyfurfuryl alcohol resin,<sup>57</sup> as well as polyetherimide films coated on  $\gamma$ -alumina tubes.<sup>58</sup> The latter membranes have exhibited significantly higher separation factors, permeance, and stability than other CMSMs prepared by other research groups. The details of their preparation and characterization are given elsewhere.<sup>58</sup> In the present paper, we present the results of MD simulation of adsorption in CMSMs using a novel model that we have developed for their pore space. Elsewhere<sup>59–61</sup> we report the results of extensive nonequilibrium MD simulations, focusing on transport of gas mixtures in the pores of CMSMs.

The plan of this paper is as follows. In the next section we describe the molecular models of PCs and CMSMs that we use in our simulations. We then discuss the details of our MD simulation method. Next, we describe a new statistical mechanical theory of adsorption that was developed recently by our group.<sup>37</sup> We then discuss the simulation results for adsorption of a variety of single gases and their binary mixtures in PCs and CMSMs, and compare them with the predictions of the statistical mechanical theory. The paper is summarized in the last section where we discuss some important remaining issues.

## Models of the Microporous Materials

We first describe the molecular model that we use for representing the pore space of PCs, after which we present the details of a novel molecular model for CMSMs.

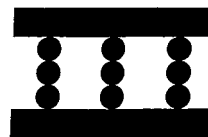


**Figure 1.** Schematic representation of the (side view of) model of pillared clays.

**A. Pillared Clays.** In the model of PCs used in this study, the tetrahedral silicate layers, which we call the solid walls, are represented by the (100) face of a face-centered cubic solid with specified surface number density. The pillars are represented by rigid chains consisting of a given number of Lennard-Jones (LJ) spheres separated by their size parameter  $\sigma_p$ . They are intercalated vertically in the space between the solid walls. The  $z$ -coordinate of the centers of the end spheres of the pillar chains is  $0.5 \times (\sigma_w + \sigma_p)$ , where  $\sigma_w$  is the size parameter of the atoms representing the solid walls. The pillars are distributed uniformly between the solid walls such that the centers of the pillars are placed at the nodes of an imaginary square lattice attached to the walls. A schematic representation of the model with a uniform distribution of the pillars and a height of  $3\sigma_p$  is given in Figure 1. For a given spatial distribution of the pillars, two parameters suffice for defining the morphology of the model. One is the interlayer spacing  $h_w$ , which is the separation between the centers of the atoms on the upper and lower layers, while the other one is the surface density of the pillars  $\rho_p$ , which is the number of pillars per unit area of the solid walls. The ideal porosity of the system is defined as the volume fraction of the system not occupied by the pillars, which is larger than the actual porosity, i.e., the volume fraction of the pore space that is accessible to the adsorbing molecules. The layer separation  $h_w$  is set to be 10.96 Å, which was obtained by adding the average pore width of Al-PC as determined by Baksh and Yang<sup>18</sup> and the size parameter  $\sigma_w$  of oxygen anions (see below). Except in the  $z$ -direction (perpendicular to the walls), periodic boundary conditions were employed.

**B. Carbon Molecular Sieve Membranes.** Pore connectivity and size distribution, pore entrance characteristics, and surface heterogeneity all play important roles in determining the transport and sorption properties of microporous materials. This is particularly true for CMSMs. To take these effects into account, we have developed a novel algorithm for generating a molecular carbon pore network using a three-dimensional (3D) Voronoi tessellation.

The network is generated by first creating a 3D simulation box of carbon atoms with a structure corresponding to graphite. We then insert into the box a predetermined number of Poisson (random) points. Each Poisson point in the box is the basis for a Voronoi polyhedron, which is that part of the space (box) that is nearer to this point than to any other. This procedure tessellates space into a set of 3D Voronoi polyhedra such that the box contains the same number of polyhedra as that of the Poisson points. To create the pore space, we fix the desired porosity and select at random a number of the polyhedra so that the ratio of their total volume and the volume of the box equals the preselected porosity. The polyhedra so chosen are then designated as the pores of the system. The carbon atoms inside these polyhedra are then removed from the simulation box, together with the dangling carbon atoms that are connected to only one neighboring carbon atom. The remaining carbon atoms inside the box constitute the solid mass of the simulated pore network structure of the membrane.

Since the pore polyhedra are selected at random, their size distribution is Gaussian. However, we can also designate the

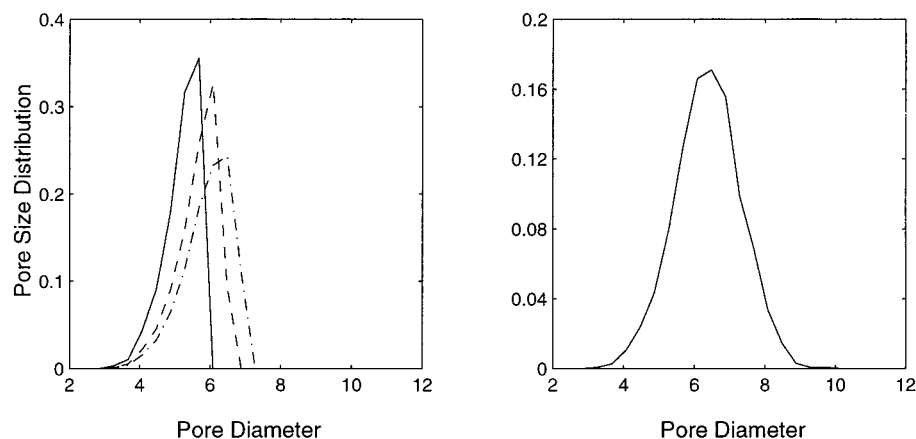


**Figure 2.** Computed pore size distribution (PSD) for the model CMSMs. On the left is the PSD for a system in which the pores are generated according to their sizes, starting from the smallest size. Solid curve is for the ideal porosity  $\varphi = 0.25$ , dashed curve for  $\varphi = 0.5$ , and dashed-dotted curve for  $\varphi = 0.7$ . On the right is the PSD for a system in which the pores are selected randomly.

pore polyhedra with a certain bias, so that the resulting size distribution would mimic the experimental shape of the pore size distribution of a real membrane. Since the goal in membrane preparation for separation processes is to create a pore space with very small pores, the pore size distribution of such membranes is typically skewed toward the smallest pores. To simulate such pore size distributions, we can proceed as follows. We first sort and list the polyhedra in the box according to their sizes, from the smallest to the largest. The size of a polyhedron is defined as the radius of a sphere with the same volume as the polyhedron. Then, to generate the pore space with the desired porosity and pore size distribution, we select the polyhedra according to their sizes, starting from the smallest ones in the list. Figure 2 compares the pore size distribution of the pore network generated by the two methods. While the pore size distribution of the system in which the pore polyhedra are selected at random is independent of the porosity, the pore size distribution that is generated with the bias toward the smaller pores is dependent upon the porosity. By controlling the box size and the number of the initial Poisson points, one can independently fix the average pore size of the pore network.

Because of the disordered structure of the molecular pore network that we generate, several important aspects of the simulations must be addressed. For example, one must average the results over a suitable number of pore network realizations in order to obtain representative results for the adsorption isotherms. In addition, for any given realization, one must also average the results over a number of initial positions of the gas molecules in the pore space in order to decrease to a reasonable level the statistical fluctuations in the results. Finally, the initial box must also be large enough in order for the results to be independent of its size.

To address these issues, we carried out some preliminary simulations in which we used equilibrium molecular dynamics (EMD) simulations (see below) to study adsorption and diffusion of  $\text{CH}_4$  through the pore networks. We found, as expected, that the larger the simulation box, the smaller the scatter in the values of the adsorption and diffusion properties among the different realizations of the molecular pore network. The differences among the realizations are also strongly dependent upon the initial loading of molecules. The lower the initial loading of the gas molecules, the more significant the effect of the initial spatial distribution of the gas molecules on the properties calculated. Of the properties calculated, the self-diffusion coefficient varied the most among the different realizations of the network and the initial spatial distribution of the gas

molecules in the pore space, while the adsorption isotherms were much less affected. Hence, we determined that for the adsorption isotherms reported in this paper, one realization of a large network (i.e., a large size of the simulation box) and large initial loading suffice to yield reasonably accurate results (the adsorption isotherms reported here were of course averaged over a few initial spatial distributions of the gas molecules in the pore space). Note that, unlike the traditional pore networks that have been used in simulation and modeling of flow and transport in porous media,<sup>7</sup> the pore networks used in this study are *molecular* networks in which the interaction of all the atoms with each other have been taken into account.

The dimensions of the simulation box we used were  $63.90 \times 63.95 \times 63.65$  Å in the  $x$ -,  $y$ -, and  $z$ -directions, respectively. The carbon atoms were packed with a structure corresponding to graphite, so that the number density of the carbon atoms was  $114 \text{ nm}^{-3}$  and the spacing between the adjacent graphite layers in the  $z$ -direction was 0.335 nm. The total initial number of carbon atoms in the simulation box was 29 640. We inserted 1800 Poisson points in the box, hence constructing a 3D Voronoi tessellation of the box containing 1800 polyhedra. We must point out that, similar to PCs, in such molecular pore networks there is a difference between the ideal porosity, i.e., the volume fraction of the polyhedra designated as the pores, and the accessible porosity, which is the volume fraction of the pores that is accessible to the gas molecules, since a number of polyhedra are isolated or their sizes are too small to accommodate the gas molecules. We have carried out our simulations at ideal porosities of 50%, 60%, and 70%. Note that, for example, for ideal porosity of 50%, the accessible porosity is only about 22%, which is just above the percolation threshold of a 3D Voronoi structure, which is about 0.16.<sup>6</sup> As a result, at this porosity the accessible pore space is barely connected. The average pore size for these pore networks is about 6.4 Å if the pore polyhedra are selected at random. The corresponding average pore sizes, when the pores are selected with a bias toward the smaller sizes, are 5.19, 5.63, and 5.92 Å, respectively, so that, as expected, the lower porosity network also has a lower average pore size when the pore polyhedra are selected with a bias toward the smaller sizes. The mean pore size of typical CMSMs that have been used in our experimental studies<sup>58</sup> is about 3.5 Å. As mentioned above, one can control the mean pore size and the pore size distribution of our model of CMSMs by adjusting the size of the simulation box and the number of Poisson points that are inserted in it. For example, with the same box size as we used in our simulation, one needs



**TABLE 1: The Three Molecular Pore Networks Used in the Simulations**

ideal porosity (%)	no. of C atoms remaining	effective porosity (%)
70	6526	0.47
60	9567	0.33
50	12781	0.22

to insert about 11 600 Poisson points (i.e., 11 600 polyhedra) in order to produce an average pore size of about 3.5 Å if the pore polyhedra are selected at random. This requires formidable computations, but it does point to the great flexibility of our model. Periodic boundary conditions were used in all three directions. The details of our simulations are summarized in Table 1.

### Molecular Dynamics Simulation

Similar to the MD simulations of gases in zeolites,<sup>62–64</sup> we have adopted the conventional assumptions of pairwise additivity and a rigid solid (i.e., the pillars and the walls in PCs and the carbon walls in CMSMs) in dealing with solid–fluid systems and describing the adsorbate–adsorbate and adsorbate–solid interactions. By rigid we mean that the solid walls or the pillars do not swell upon adsorption of the gas molecules, and the vibrational motions of the atoms in the solid are ignored. We used the standard cut-and-shifted LJ potential

$$\phi(r) = \begin{cases} \phi_{\text{LJ}}(r) - \phi_{\text{LJ}}(r_c) & \text{if } r \leq r_c \\ 0 & \text{if } r > r_c \end{cases} \quad (1)$$

to describe the interactions between the adsorbates, as well as between them and the spheres that comprise the pillars or the carbon atoms in the CMSMs, where  $r$  is the separation between interacting pairs,  $r_c$  is the truncation distance of the potential, and  $\phi_{\text{LJ}}$  is the standard LJ 6–12 potential, with  $\epsilon$  and  $\sigma$  as the usual energy and size parameters, respectively; the value of  $r_c$  was taken to be  $5\sigma_{\text{CH}_4}$ . In the simulations for PCs, the interaction between the adsorbates and the solid walls was approximated by the well-known 10–4–3 potential of Steele<sup>65</sup>

$$\phi_w = 2\pi \rho_w \epsilon_w \sigma_w^2 \Delta \left[ \frac{2}{5} \left( \frac{\sigma_w}{z} \right)^{10} - \left( \frac{\sigma_w}{z} \right)^4 - \frac{\sigma_w^4}{3\Delta (z + 0.61\Delta)^3} \right] \quad (2)$$

where  $\epsilon_w$  and  $\sigma_w$  are the energy and size parameters characterizing the interactions between the adsorbates and the atoms that comprise the solid walls, and  $z$  is the vertical distance from the walls. In the simulations for CMSMs, the interaction between the gas molecules with the whole carbon pore network was the sum of the LJ potentials between the gas molecules and each individual carbon atom in the network. The total potential energy of the system for, e.g., the PCs, can then be written as

$$\Phi = \frac{1}{2} \sum_i^N \sum_j^N \phi_{\text{LJ}}(r_{ij}; \sigma_0, \epsilon_0) + \sum_i^N [\phi_w^{(L)}(z_i; \sigma_w, \epsilon_w) + \phi_w^{(U)}(z_i; \sigma_w, \epsilon_w)] + \sum_i^N \sum_k^{N_p} \phi_{\text{LJ}}(r_{ik}; \sigma_k, \epsilon_k) \quad (3)$$

where  $N_p$  is the number of the pillars,  $N$  is the number of the adsorbing molecules, and superscripts  $L$  and  $U$  are used to

distinguish between the potential energies associated with the lower and the upper silicate layers. A similar expression was used in the simulations of CMSMs.

The EMD simulations were performed in the microcanonical ensemble with periodic boundary conditions as specified above. For PCs the trajectories of the molecules were generated by solving Newton's equation of motion using a standard fifth-order predictor–corrector method.<sup>66,67</sup> For this system the trajectories of the adsorbate molecules were collected in a typical duration of 50 000 time steps, after spending about  $10^4$  time steps for system equilibration. For CMSMs we used Verlet's velocity algorithm<sup>66,67</sup> to find the particles' trajectories. This also allowed us to compare the performance of the two methods for determining the particles' trajectories. The accuracy of the two methods were comparable. The trajectories of the particles were collected in a typical duration of  $4 \times 10^5$  time steps, after discarding the first  $4 \times 10^5$  time steps for equilibration of the system.

The chemical potentials (to be used in the comparison with the predictions of the statistical mechanical theory; see below) were calculated using Widom's test particle method.<sup>68–71</sup> At the beginning of each simulation run, the simulation cell was divided into a large number of small subcells and a test particle was assigned to each subcell. For example, for adsorption simulations in CMSMs, the simulation box was discretized into  $n_x \times n_y \times n_z$  grid points along the  $x$ -,  $y$ -, and  $z$ -directions, respectively, where  $n_x = n_y = n_z = 111$ , thus resulting in over 1 367 000 small subcells. The test particle–solid interaction energies and their three derivatives, associated with all the subcells, were then calculated and recorded. They also served as the grid point values for the interpolation calculations described below. The test particles whose interaction energies in units of  $k_B T$  (where  $k_B$  is the Boltzmann's constant) were less than a certain positive value  $\epsilon$  (for example, 20) were considered as “active” test particles, and those with interaction energies larger than  $\epsilon$  were considered “idle” states, since they make essentially no contribution to the chemical potential:

$$\beta \mu_{ci} = \ln(\rho x_i) - \ln \langle \exp[-\beta U_i(\mathbf{r}_i)] \rangle \quad (4)$$

Here  $\rho$  is the total number density,  $x_i$  is the mole fraction of component  $i$ ,  $U_i$  is the potential energy of a test particle of type  $i$ ,  $\mu_{ci}$  is the configurational chemical potential, and  $\langle \cdot \rangle$  denotes an average over time and active test particles. For simplicity, in the remainder of this paper, we will simply use  $\mu_i$  to denote  $\mu_{ci}$  and refer to it as the chemical potential.

For computing the chemical potentials and the adsorption isotherms in PCs, at each sampling step typically 10% of the active test particles were randomly selected, which proved sufficient for all the PCs porosities used in the simulations. Depending on the loading of the adsorbate molecules and the size of the simulation cell, the number of the active test particles varied from 8000 to 12 000. The corresponding numbers for CMSMs were 0.5% of the active test particles for 70% (ideal) porosity and 1% of them for 60% and 50% porosities, which typically resulted in random selection of about 2000–4000 of the active particles. Energy conservation in the system was monitored in each simulation, and the time step was adjusted according to the loading of the adsorbate molecules and the size of the pores, such that the standard deviations of the total energy relative to the mean was about  $5 \times 10^{-4}$  or less. Typical value of the time steps selected in this way was  $5 \times 10^{-3}$  in the reduced unit of  $\text{CH}_4$  (see below), or  $7.37 \times 10^{-3}$  ps.

In the CMSMs simulations, to reduce the simulation time for calculating the interaction between a gas molecule and all

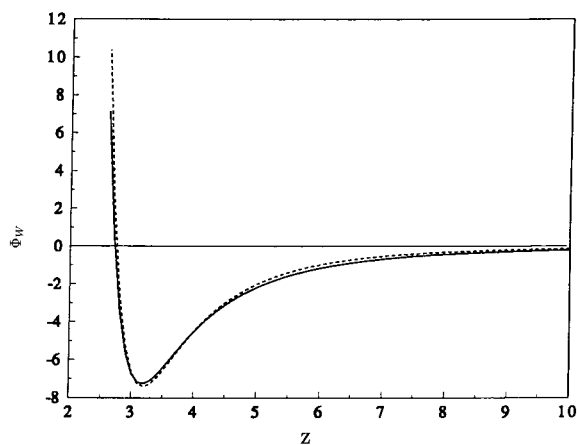


**Figure 3.** Potential energy (in kJ/mol) of the aluminum pillared clays/nitrogen system. Dashed curve is from ref 19, while the full curve is the 10-4-3 potential, eq 2.

**TABLE 2: Values of the LJ Parameters Used in the Simulations**

atom	$\sigma$ (Å)	$\epsilon/k_B$ (K)	mass (a.m.u)
CH <sub>4</sub>	4.010	142.87	16.040
CO <sub>2</sub>	4.328	198.20	44.010
CF <sub>4</sub>	4.744	151.50	88.005
N <sub>2</sub>	3.700	95.05	28.030
C(graphite)	3.400	28.00	

the carbon atoms in the molecular network, we used a 3D piecewise cubic Hermite interpolation<sup>72,73</sup> to compute the potential energy and forces for the gas particle at any position using the previously recorded information at the  $n_x \times n_y \times n_z$  grid points. The Hermite method interpolates a function and its three first derivatives and proved to yield accurate results using the grid point values.

We have studied adsorption of CH<sub>4</sub>, CO<sub>2</sub>, CF<sub>4</sub>, and N<sub>2</sub>, as well as three binary mixtures, CH<sub>4</sub>–N<sub>2</sub>, CO<sub>2</sub>–N<sub>2</sub>, and CF<sub>4</sub>–N<sub>2</sub>. The four gases were assumed to be LJ spheres to which we assigned the effective values of the LJ size and energy parameters,  $\sigma$  and  $\epsilon$ . These values as well as those for the graphite carbon atoms used in the CMSMs simulations are summarized in Table 2. For PCs, the size parameter  $\sigma_w$  of oxygen anions on the silicate layers used was 2.74 Å. The energy parameter  $\epsilon_{wN_2}$  for wall–nitrogen interaction was determined by fitting eq 2 to the potential profile of the same system reported in the literature,<sup>17</sup> which was deduced from adsorption data using the Jaroniec–Choma method<sup>74</sup> and the Horvath–Kawazoe model<sup>75</sup> for slit pores. The potential energy fitted to eq 2 with  $\sigma_{wN_2}/k_B = 26.2$  K, and the potential profile obtained from the experimental data are both plotted in Figure 3. To estimate the potential parameter  $\epsilon_{wX}$  for any other gas X, we used the Lorentz–Berthelot rule according to which

$$\epsilon_{wN_2} = \sqrt{\epsilon_w \epsilon_{N_2}} \quad (5)$$

$$\epsilon_{wX} = \sqrt{\epsilon_w \epsilon_X} \quad (6)$$

Therefore

$$\epsilon_{wX} = \epsilon_{wN_2} \sqrt{\frac{\epsilon_X}{\epsilon_{N_2}}} \quad (7)$$

so that from knowledge of  $\epsilon_X$ ,  $\epsilon_{N_2}$ , and the fitted value of  $\epsilon_{wN_2}$ , any other  $\epsilon_{wX}$  can be computed. This rule was used in calculating all other cross-interaction parameters. The resulting potential

**TABLE 3: Potential Parameters for the Mixtures in the Simulations of Pillared Clays**

pair	$\sigma$ (Å)	$\epsilon/k_B$ (K)
methane–methane	4.01	142.87
nitrogen–nitrogen	3.70	95.05
methane–wall	3.375	32.12
nitrogen–wall	3.22	26.20
methane–pillar	3.375	32.12
nitrogen–pillar	3.22	26.20

**TABLE 4: Conversion Factors between the Dimensionless and the Actual Quantities**

variable	dimensionless form
length $L$	$L^* = L/\sigma_{CH_4}$
energy $U$	$U^* = U/\epsilon_{CH_4}$
mass $M$	$M^* = M/M_{CH_4}$
density $\rho$	$\rho^* = \rho\sigma_{CH_4}^3$
temperature $T$	$T^* = k_B T/\epsilon_{CH_4}$
pressure $P$	$P^* = P\sigma_{CH_4}^3/\epsilon_{CH_4}$
time $t$	$t^* = t(\epsilon_{CH_4}/M_{CH_4} \sigma_{CH_4}^2)^{1/2}$

parameters for CH<sub>4</sub>, N<sub>2</sub>, the pillars, and the walls are listed in Table 3, which can be used for calculating those for the other gases. The atomic density of the clay sheet  $\rho_w$  of PCs and the distance between the atomic layers within the clay sheet  $\Delta$  were chosen to be 3.038 Å<sup>-3</sup> and 2.16 Å, respectively, which are typical values for these materials.<sup>76</sup>

For simplicity, physical quantities are expressed in reduced units, that is, the energy and size parameters  $\epsilon_{CH_4}$  and  $\sigma_{CH_4}$  of methane were used as the basic units of energy and length. The conversion factors that convert the dimensionless parameters (denoted by \*) to dimensional quantities for temperature, pressure, energy, density, and time are listed in Table 4.

### Statistical Mechanical Theory of Adsorption

Before presenting the simulations results, and in order to correlate and predict them, we describe the essence of a new statistical mechanical theory of adsorption of gases in porous materials that was developed recently by us.<sup>37</sup>

We first consider adsorption of a single gas. Consider a porous material that is immersed in a pure fluid, characterized macroscopically by its temperature  $T$  and the chemical potential  $\mu$ . At equilibrium the temperatures and the chemical potentials of the molecules in both the solid material and the fluid phases are equal, and the net flux of the molecules across the phase boundary must vanish. The marginal probability density of observing the solid system to have  $N$  molecules inside is

$$P(N, T) = \frac{\exp(N\beta\mu)}{\Xi} Q \quad (8)$$

where  $\beta = (k_B T)^{-1}$ , and  $Q(N, T, V)$  and  $\Xi(\mu, T, V)$  are the usual canonical and grand-canonical partition functions of the system, respectively

$$Q(N, T, V) = \frac{1}{N! \lambda^{3N}} \int \exp[-\beta \Phi(\mathbf{r}^N)] d\mathbf{r}^N \quad (9)$$

$$\Xi(\mu, T, V) = \sum_{N=0}^{\infty} \exp(N\beta\mu) Q(N, T, V) \quad (10)$$

where  $V$  is the volume of the system,  $\lambda$  is the thermal wavelength of the molecules,  $\Phi(\mathbf{r}^N)$  is the potential energy of the system, and  $\mathbf{r}^N$  is the abbreviation for  $(\mathbf{r}_1, \mathbf{r}_2, \dots, \mathbf{r}^N)$ , representing the positions of all the  $N$  molecules in the system. Assuming that

the solid is rigid, and that the potential energy can be partitioned into molecule–molecule ( $\Phi_0$ ) and molecule–solid ( $\Phi_s$ ) contributions,  $\Phi(\mathbf{r}^N) = \Phi_0(\mathbf{r}^N) + \Phi_s(\mathbf{r}^N)$ , we can write

$$Q(N, T, V) = \frac{1}{N! \lambda^{3N}} \int \exp\{-\beta[\Phi_0(\mathbf{r}^N) + \Phi_s(\mathbf{r}^N)]\} d\mathbf{r}^N = Q_0 \langle \exp[-\beta\Phi_s(\mathbf{r}^N)] \rangle_0 = Q_0 F_s \quad (11)$$

Here  $Q_0(N, T, V)$  is the canonical partition function of the bulk fluid and  $\langle \cdot \rangle_0$  denotes an average in the ensemble of the bulk fluid.

In the absence of a phase transition, which in adsorptive porous materials usually occurs at temperatures that are low compared to the bulk temperature (see, however, below for further discussion of this point), the density fluctuations are negligibly small, and the average density corresponds to the value that maximizes the probability density  $P(N, T)$  in the particle number and the configuration space, namely

$$\left[ \frac{\partial}{\partial N} P(N, T) \right]_{N=N_s} = 0 \quad (12)$$

or equivalently

$$\left[ \frac{\partial}{\partial N} \ln P(N, T) \right]_{N=N_s} = 0 \quad (13)$$

which means that

$$\left[ \frac{\partial}{\partial N} \ln Q_0(N, V, T) \right]_{N=N_s} + \left[ \frac{\partial}{\partial N} \ln \langle \exp(-\beta\Phi_s) \rangle_0 \right]_{N=N_s} = -\beta\mu \quad (14)$$

where  $N_s = \langle N \rangle$ . Since the Helmholtz free energy  $A_0$  is related to the partition function by  $A_0(N, V, T) = -k_B T \ln Q_0(N, V, T)$ , we have

$$\left[ \frac{\partial}{\partial N} \ln Q_0(N, V, T) \right]_{N=N_s} = -\beta\mu_0(T, \rho_s) \quad (15)$$

where  $\rho_s = N_s/V$ . Because at equilibrium the adsorbate chemical potential is identical to the bulk fluid chemical potential,  $\mu = \mu_0(T, \rho_0)$ , we can write eq 14 as

$$\beta\mu_0(T, \rho_s) - \beta\mu_0(T, \rho_0) = \left( \frac{\partial}{\partial N} \ln F_s \right)_{N_s} \quad (16)$$

which establishes an implicit relation between the equilibrium loading  $\rho_s$  and the macroscopic state  $(T, \rho_0)$  of the bulk fluid, where  $F_s$  is a function of equilibrium loading.

We now assume that  $F_s$  can be written as the  $N$ th power of a polynomial in equilibrium loading  $\rho_s$  at a given temperature, namely

$$F_s = \langle \exp[-\beta\Phi_s(\mathbf{r}^N)] \rangle_0 = (c_0 + c_1\rho_s + c_2\rho_s^2 + \dots)^N \quad (17)$$

Therefore

$$\beta\mu_0(T, \rho_s) - \beta\mu_0(T, \rho_0) = \ln \left( \sum_{i=0} c_i \rho_s^i \right) + \frac{\sum_{i=0} i c_i \rho_s^i}{\sum_{i=0} c_i \rho_s^i} \quad (18)$$

The leading term  $c_0$  can be obtained easily. When the system is infinitely dilute [ $\rho \rightarrow 0$  and  $\phi_0(\mathbf{r}^N) \rightarrow 0$ ], we can write

$$F_s = \frac{1}{V^N} \prod_{i=1}^N \int \exp[-\beta\Phi_{i,s}(\mathbf{r}_i)] d\mathbf{r}_i \quad (19)$$

Comparing this equation with eq 16 under the condition  $\rho \rightarrow 0$  gives

$$c_0 = \frac{1}{V} \int \exp[-\beta\Phi_{i,s}(\mathbf{r}_i)] d\mathbf{r}_i \quad (20)$$

Hence, for a given  $T$  and configuration of the pore space,  $c_0$  can be determined simply from eq 20. Therefore, the working equation for adsorption of a single gas is given by

$$\beta\mu_0(T, \rho_s) - \beta\mu_0(T, \rho_0) = \ln \left( c_0 + \sum_{i=1} c_i \rho_s^i \right) + \frac{\sum_{i=1} i c_i \rho_s^i}{c_0 + \sum_{i=1} c_i \rho_s^i} \quad (21)$$

One can easily check that the above result will reduce, in the limit of infinite dilution, to the equation of state (EOS) of noninteracting gases, subject to an external field, as it should be.

Consider now a binary sorption system whose canonical partition function can be written as

$$Q(N_a, N_b, T, V) = \frac{1}{N_a! N_b! \lambda_a^{3N_a} \lambda_b^{3N_b}} \int \exp[-\beta(\Phi_{aa} + \Phi_{as} + \Phi_{bb} + \Phi_{bs} + \Phi_{ab})] d\mathbf{r}_a^{N_a} d\mathbf{r}_b^{N_b} \quad (22)$$

where  $\Phi_{aa}$ ,  $\Phi_{as}$ ,  $\Phi_{bb}$ ,  $\Phi_{bs}$ , and  $\Phi_{ab}$  are potential energies associated with a–a, a–solid, b–b, b–solid, and a–b interactions, respectively, and a and b represent the two gases. As we show below, the pure component adsorption can be adequately represented by utilizing a simple truncated series, and therefore we concentrate here in relating the mixture properties to those of pure components. We rewrite eq 22 as

$$Q(N_a, N_b, T, V) = Q_a(N_a, T, V) Q_b(N_b, T, V) \langle \exp(-\beta\Phi_{ab}) \rangle_s \quad (23)$$

where  $Q_a$  and  $Q_b$  are the canonical partition functions of pure component sorption systems. The subscript  $s$  stands for a canonical ensemble in which the interaction between  $a$  and  $b$  has been turned off, namely

$$\langle \exp(-\beta\Phi_{ab}) \rangle_s = \frac{\int \exp(-\beta\Phi_{ab}) \exp(-\beta\Phi') d\mathbf{r}_a^{N_a} d\mathbf{r}_b^{N_b}}{\int \exp(-\beta\Phi') d\mathbf{r}_a^{N_a} d\mathbf{r}_b^{N_b}} \quad (24)$$

where

$$\Phi' = \Phi_{aa} + \Phi_{bb} + \Phi_{as} + \Phi_{bs} \quad (25)$$

When the loading is low, the adsorbate–adsorbate interaction energy is small compared with that of the adsorbate–adsorbent, i.e.,  $\langle \exp(-\beta\Phi_{ab}) \rangle_s \approx 1$ , which reduces eq 23 to

$$Q(N_a, N_b, T, V) = Q_a(N_a, T, V) Q_b(N_b, T, V) \quad (26)$$

from which the following isotherms can be obtained directly

$$\beta\mu_a^m(T, \rho_a, \rho_b) = \beta\mu_a(T, \rho_a) \quad (27)$$

$$\beta\mu_b^m(T, \rho_a, \rho_b) = \beta\mu_b(T, \rho_b) \quad (28)$$

where  $\mu_i^m(T, \rho_a, \rho_b)$  ( $i = a$  or  $b$ ) is the chemical potential of component  $i$  in the adsorbed phase consisting of the mixture and the adsorbent, while  $\mu_i(T, \rho_i)$  is the chemical potential of pure adsorbed component  $i$ .

As the loading is increased, the interaction between the unlike adsorbate molecules can no longer be neglected. To take this cross-interaction into account, we assume a form typical of regular solutions

$$\langle \exp(-\beta\Phi_{ab}) \rangle_s = (1 - \rho_a\rho_b/\kappa_{ab}^2)^{N_a+N_b} \quad (29)$$

where  $\kappa_{ab}$  is a constant to be determined, or else be treated as an adjustable parameter. Clearly, eq 29 has the required correct asymptotic behavior:  $\lim_{\rho_i \rightarrow 0} \langle \exp(-\beta\Phi_{ab}) \rangle_s = 1$ . From eq 29 the following isotherms are then derived

$$\begin{aligned} \beta\mu_a^m(T, \rho_a, \rho_b) - \beta\mu_a(T, \rho_a) = \\ -\ln(1 - \rho_a\rho_b/\kappa_{ab}^2) + \frac{\rho\rho_b/\kappa_{ab}^2}{1 - \rho_a\rho_b/\kappa_{ab}^2} \quad (30) \end{aligned}$$

$$\begin{aligned} \beta\mu_b^m(T, \rho_a, \rho_b) - \beta\mu_b(T, \rho_b) = \\ -\ln(1 - \rho_a\rho_b/\kappa_{ab}^2) + \frac{\rho\rho_a/\kappa_{ab}^2}{1 - \rho_a\rho_b/\kappa_{ab}^2} \quad (31) \end{aligned}$$

In many adsorption systems, the adsorbate–adsorbate interactions are weak compared to adsorbate–adsorbent interactions. Furthermore, if the unlike pair adsorbate–adsorbate interactions are approximated by some sort of average of the like pair adsorbate–adsorbate interactions (i.e., the bulk fluid mixture acts as an ideal solution), then we can expect the adsorbate phase also to be ideal-solution-like. In this case, the chemical potentials are given simply as

$$\beta\mu_a = \beta\mu_a^0 + \ln x_a \quad (32)$$

$$\beta\mu_b = \beta\mu_b^0 + \ln x_b \quad (33)$$

where  $\mu_a^0$  and  $\mu_b^0$  are the chemical potentials of adsorbed  $a$  and  $b$  in the single-component system, evaluated at the same *total* loading  $\rho = \rho_a + \rho_b$  as for  $\mu_a$  or  $\mu_b$ .

We now use these isotherms to correlate our simulation results for adsorption of pure gases as well as their mixtures.

### Molecular Dynamics Results and Comparison with Theory

We first discuss the results for adsorption in CMSMs, after which we present those for PCs.

**A. Adsorption in Carbon Molecular Sieve Membranes.** Before proceeding with studies of adsorption of gas mixtures, we first evaluate the properties of the single-component adsorption behavior for the four gases and also apply the statistical mechanical theory of adsorption described above to correlate the data. The simulated adsorption isotherms for the four gases at three different porosities are shown in Figures 4–6, where they are also compared with the predictions of our statistical mechanical theory, eq 21. In all cases, we calculated  $c_0$  from eq 20 and fitted the simulation results to eq 21 using  $c_1$  as the only adjustable parameter. The simulations were carried out at  $T = 298$  K. As these figures indicate, for porosities 70% and 60% the theory represents the data very accurately up to the loading  $\rho = 0.15$ , although higher loadings were also predicted equally accurately. In fact, except for  $\text{CF}_4$ , the agreement

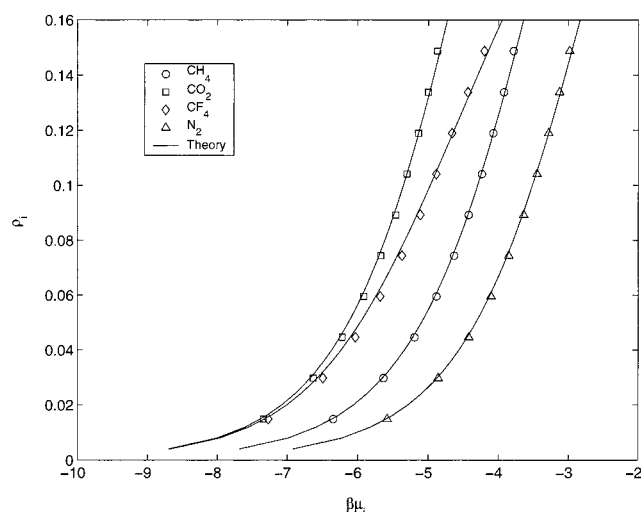


**Figure 4.** Adsorption isotherms for single gases in CMSMs at the ideal porosity of  $\varphi = 0.7$ . Symbols are the EMD simulation results, while solid curves show the theoretical predictions.  $\mu_i$  and  $\rho_i$  are the chemical potential and loading of component  $i$ , respectively, and  $\beta = (k_B T)^{-1}$ .

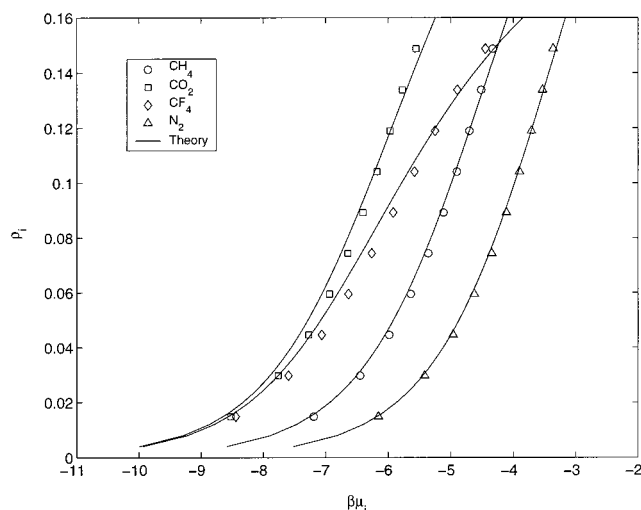


**Figure 5.** Same as in Figure 4, but for the ideal porosity  $\varphi = 0.6$ .

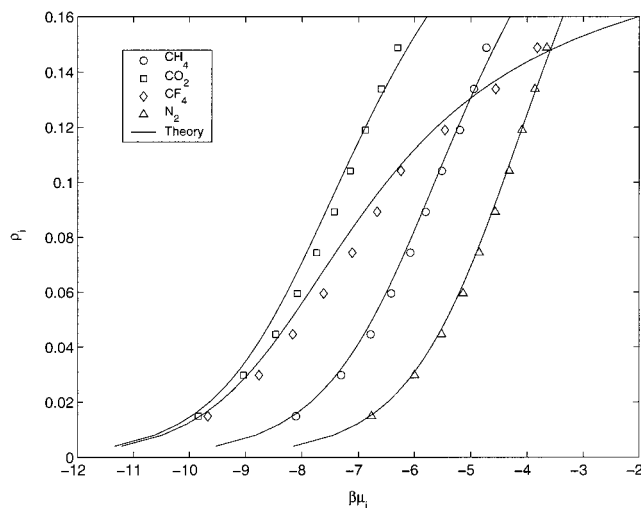


**Figure 6.** Same as in Figure 4, but for the ideal porosity  $\varphi = 0.5$ .

between the predictions and the simulation results for all the three porosities is excellent. In the case of  $\text{CF}_4$ , the agreement between the predictions and the simulation results is also



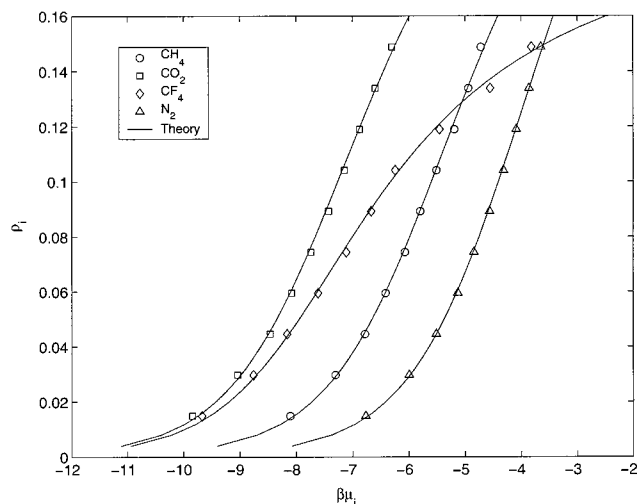


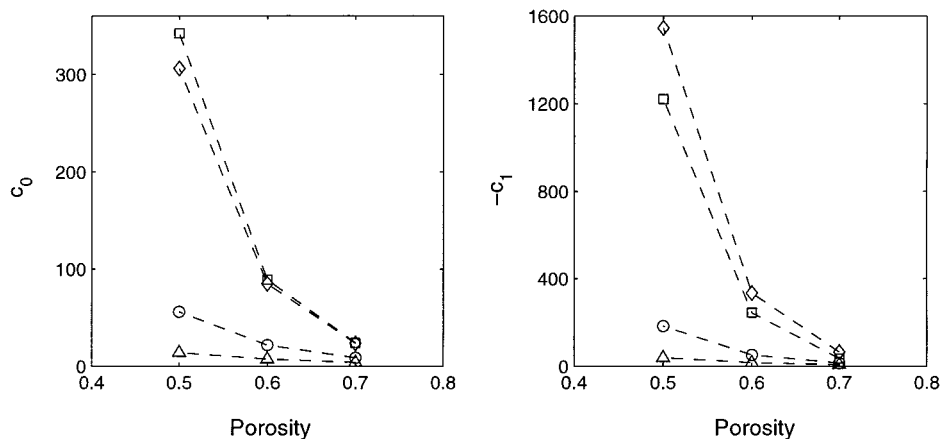
**Figure 7.** Same as in Figure 6, except that the parameter  $c_0$  has been fitted to the simulation data.

excellent at porosity  $\varphi = 0.7$ , while for  $\varphi = 0.6$  and  $0.5$  there is only a small difference between the predictions and the EMD results. We remind the reader that, with an ideal porosity of  $0.50$ , the accessible porosity is only  $0.22$ , not too far from the percolation threshold of a pore space with a structure similar to a Voronoi tessellation that is about<sup>6,7</sup>  $0.16$ , so that, unlike most mean-field-like theories,<sup>6</sup> ours is accurate even near the percolation threshold. Note also that, had we also treated  $c_0$  as an adjustable parameter, the theoretical predictions for  $\text{CF}_4$ , even at porosity  $\varphi = 0.5$ , would have been very accurate; this is shown in Figure 7. Of course, calculating  $c_0$ , instead of treating it as an adjustable parameter, makes the theory more attractive, particularly in light of the fact that the difference between the predictions for two cases is not large.

Note that, if we consider the limit  $\rho_s \rightarrow 0$  using only the  $c_0$  term, which corresponds to a constant chemical potential shift (i.e.,  $\Delta\mu$  independent of loading), we find that the predictions fail at very low loadings, which is also the range of validity of Henry's law if we use a theoretically calculated Henry's constant (which is in fact related to  $c_0$ ). However, as we demonstrated before<sup>37</sup> for the  $\text{CH}_4\text{--N}_2$  mixtures in PCs, even when Henry's law can provide a reasonable description of the data (which is the case for ideal and near ideal systems), our theory is valid over a wider range than that predicted by the Henry's law. This clearly illustrates the superiority of eq 21, where the use of a single fitted parameter,  $c_1$ , yields excellent representation of adsorption data over a wide range of the porosities. The reason

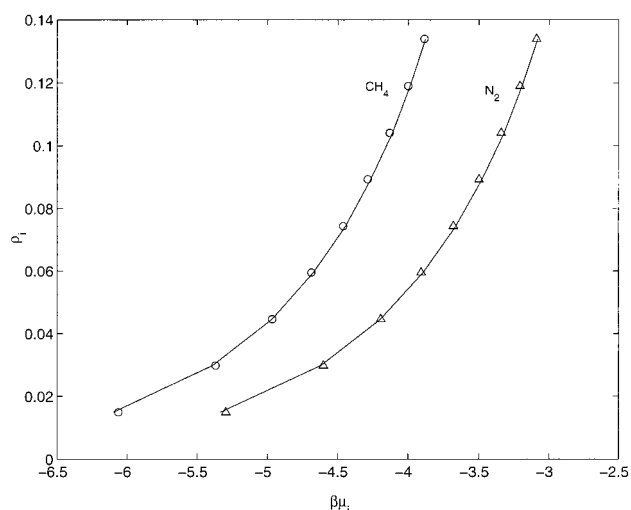
for the superior performance of eq 21 is twofold. (1) We have separated the strictly zero density behavior (represented by  $c_0$ ) and lumped the higher density behavior in  $c_1$ . (2) We have utilized adsorbate–adsorbate interaction information embedded in the bulk fluid equation of state, which is very often known quite precisely. We note also that previous studies of adsorption of simple molecules in zeolites indicate that the data cannot be adequately represented by a virial expansion of up to five terms.<sup>77–79</sup> Therefore, we conclude that short of performing the actual simulations, our statistical mechanical theory of adsorption with one adjustable parameter is a very useful alternative. The agreement between the simulation results and the predictions of the statistical mechanical theory also implies that the chemical potential can serve as an appropriate correlating variable for adsorption data, and that at least for the adsorbent–adsorbate systems studied here, data at low loadings can be used to predict behavior at higher loadings, using eq 21 with calculated  $c_0$  and adjusted  $c_1$ . One can of course easily convert the chemical potentials obtained from the simulations to pressure using an empirical EOS for the LJ fluid<sup>80</sup> and present the results in terms of the loading versus pressure curves, the traditional form of representing experimental adsorption isotherms.

Figure 8 presents the porosity dependence of  $c_0$  and  $c_1$ .  $c_0$  is positive and should be zero at the percolation threshold because the repulsive forces due to the walls prevent adsorption. Therefore, had we carried out simulations at ideal porosities less than  $0.5$ , the corresponding values of  $c_0$  would have approached  $0$ . However, carrying out the simulations at such low porosities is very difficult, as it requires very large computing times. As the porosity increases, so does  $c_0$  until it reaches a maximum where adsorption is enhanced owing to the attractive interactions exerted by the walls.  $c_0$  declines, however, with further increase in the porosity because the walls are now much further apart (since at high porosities the pore polyhedra join and make much larger pores with their walls farther apart) and thus exert a weaker attraction on the gas particles and hence their adsorption rates reduce. As the porosity approaches  $1$ , one also has  $c_0 \rightarrow 1$ , since absence of the walls implies that  $\exp(-\beta\Phi_{i,s}) \rightarrow 0$ . On the other hand,  $c_1$  is negative and, similar to  $c_0$ , approaches zero at the percolation threshold. This is expected since the total adsorption at the percolation threshold must be zero. Similar to  $c_0$ , it should also exhibit a minimum (or maximum in magnitude) at low porosities and then decay with increasing porosity, although unlike  $c_0$  the limiting value of  $c_1$  as  $\varphi \rightarrow 1$  may depend on the gases considered, since  $c_1$  acts only as an adjustable parameter. Values of  $c_0$  and  $c_1$  for  $\text{CO}_2$  and  $\text{CF}_4$  are essentially equal, which is expected as the LJ



**Figure 8.** Porosity dependence of the parameters  $c_0$  and  $c_1$  for single gases  $\text{CH}_4$  (circles),  $\text{CO}_2$  (squares),  $\text{CF}_4$  (diamonds), and  $\text{N}_2$  (triangles). Dashed lines are a guide to the eye.





**Figure 9.** Adsorption isotherms for a binary mixture of CH<sub>4</sub>–N<sub>2</sub> at the ideal porosity  $\varphi = 0.7$  in CMSMs.  $\mu_i$  denotes the chemical potential of  $i$  and  $\beta (k_B T)^{-1}$ . Symbols show the EMD simulation results, while solid curves indicate the theoretical predictions.

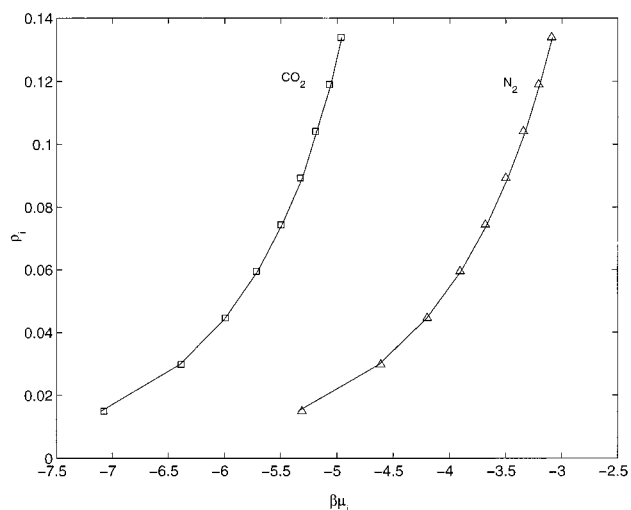


**Figure 10.** Same as in Figure 9, but for a CO<sub>2</sub>–N<sub>2</sub> mixture.

parameters for these molecules are also close to each other. The same is also true for N<sub>2</sub> and CH<sub>4</sub>. However, there is a significant difference between values of  $c_0$  and  $c_1$  for CO<sub>2</sub> and CF<sub>4</sub> on one hand, and those for N<sub>2</sub> and CH<sub>4</sub> on the other hand.

We now present the results for adsorption of binary gas mixtures. In these simulations we fixed the total loading at 0.16, where the total loading is defined as the total number of gas molecules in the pore space divided by the volume of the box. Figures 9–11 depict the adsorption isotherms for the three mixtures at an ideal porosity of  $\varphi = 0.7$  and  $T = 298$  K. In this case, similar to CMSMs, there is only one adjustable parameter,  $\kappa_{ab}$ , defined by eqs 30 and 31. As these figures demonstrate, the agreement between the simulation results and the theoretical predictions is excellent. Equally good agreement is also obtained at the ideal porosity of 0.6; see Figures 12–14. Figure 15 shows the results for the CH<sub>4</sub>–N<sub>2</sub> mixtures at the ideal porosity of 0.5. In this case there are very small differences between the simulation results and the theoretical predictions. They become larger as the difference between the LJ size parameters of the two gases increases. This is confirmed if we compare Figure 15 with the adsorption isotherms shown in Figures 16 and 17 for the ideal porosity of 0.5. While the predictions for CH<sub>4</sub>–N<sub>2</sub> (Figure 15) are still very accurate, those for the CO<sub>2</sub>–N<sub>2</sub>

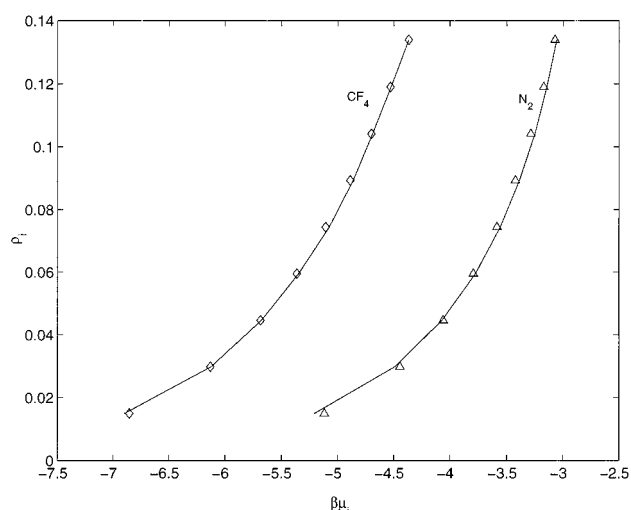


**Figure 11.** Same as in Figure 9, but for a CF<sub>4</sub>–N<sub>2</sub> mixture.

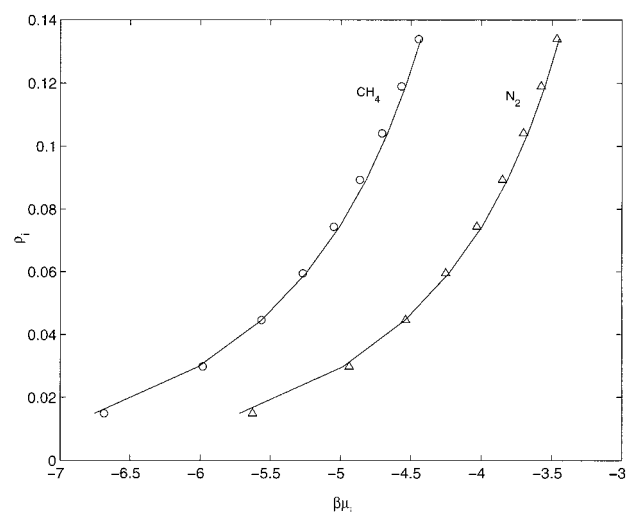


**Figure 12.** Adsorption isotherms for a binary mixture of CH<sub>4</sub>–N<sub>2</sub> at the ideal porosity  $\varphi = 0.6$  in CMSMs. Symbols show the EMD simulation results, while solid curves indicate the theoretical predictions.

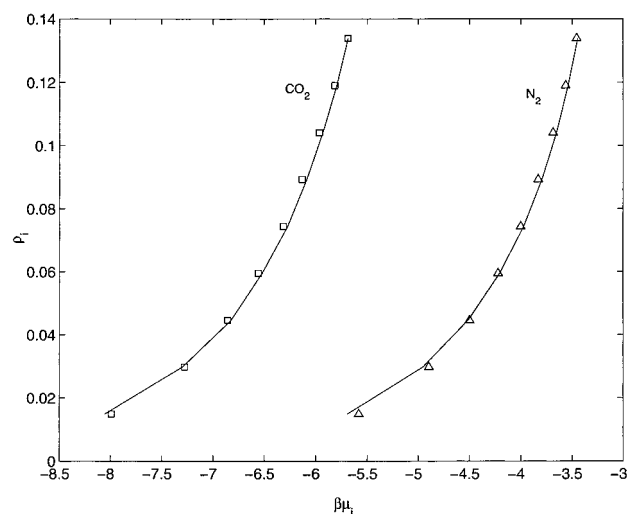


**Figure 13.** Same as in Figure 12, but for a binary mixture of CO<sub>2</sub>–N<sub>2</sub>.

and CF<sub>4</sub>–N<sub>2</sub> mixtures shown in Figures 16 and 17, which were obtained for the same ideal porosity of 0.5, exhibit some differences between the predictions and the simulation results. However, as Figure 17 indicates, the adsorption isotherm for

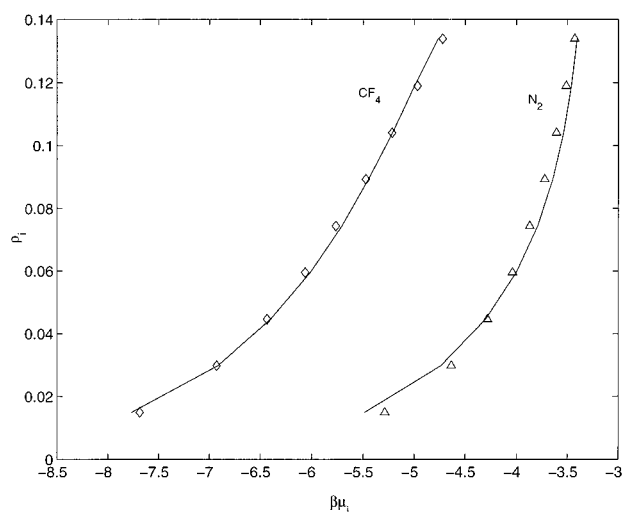


**Figure 14.** Same as in Figure 12, but for a binary mixture of  $\text{CF}_4$ – $\text{N}_2$ .

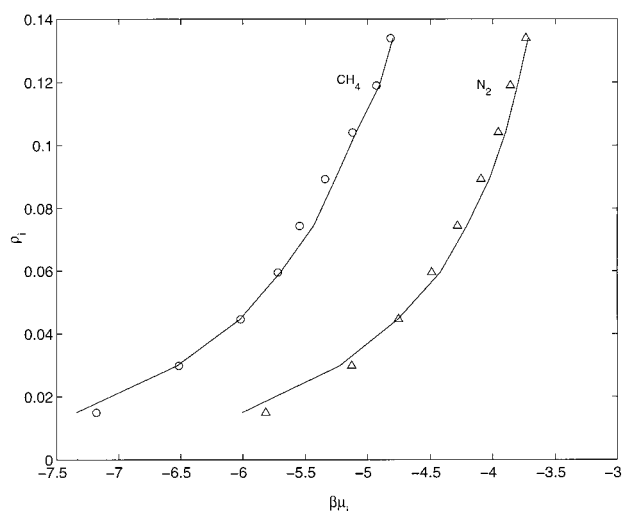


**Figure 15.** Adsorption isotherms for a binary mixture of  $\text{CH}_4$ – $\text{N}_2$  at the ideal porosity  $\varphi = 0.5$  in CMSMs. Symbols show the EMD simulation results, while solid curves indicate the theoretical predictions.

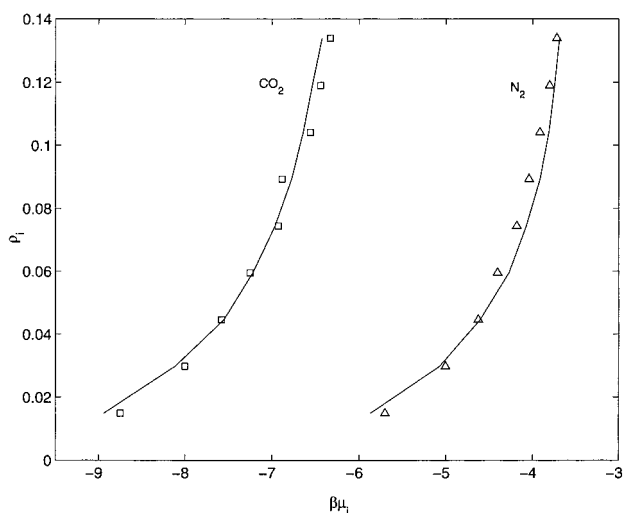


**Figure 16.** Same as in Figure 15, but for a binary mixture of  $\text{CO}_2$ – $\text{N}_2$ .

$\text{N}_2$  is very steep, indicating the closeness of the system to condensation, which represents a first-order phase transition, which is a discontinuous phase transition. As is well-known in

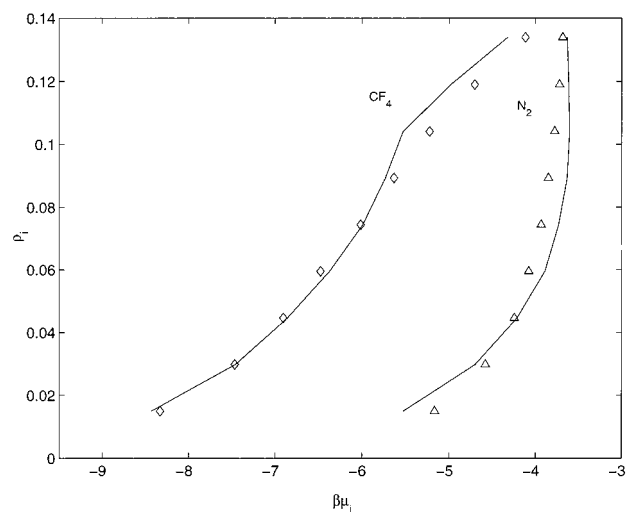


**Figure 17.** Same as in Figure 15, but for a binary mixture of  $\text{CF}_4$ – $\text{N}_2$ . The discontinuity indicates the theoretical prediction for a first-order phase-transition point (condensation).

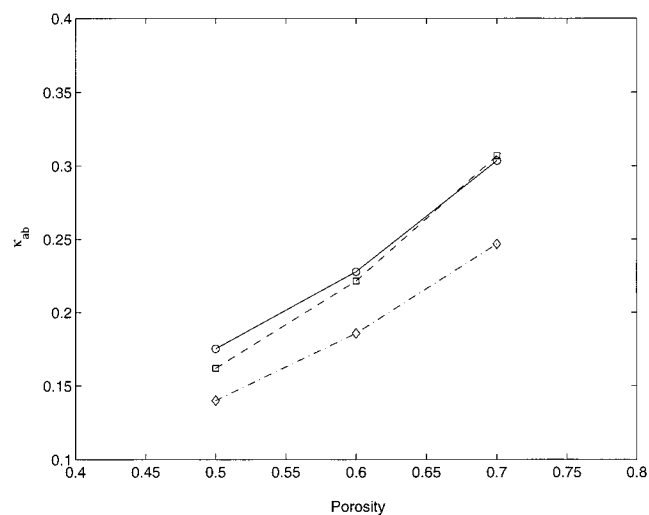


**Figure 18.** Porosity dependence of the binary interaction parameter  $\kappa_{ab}$  for  $\text{CH}_4$ – $\text{N}_2$  (circles),  $\text{CO}_2$ – $\text{N}_2$  (squares), and  $\text{CF}_4$ – $\text{N}_2$  (diamonds) mixtures. Dashed lines are a guide to the eye.

the theory of critical phenomena, mean-field-like theories are usually not very accurate near phase-transition points. Despite this, all the qualitative features of the  $\text{N}_2$  isotherm are correctly predicted by the theory. In the case of  $\text{CF}_4$ , however, we have a completely different situation. The agreement between the theory and the simulation results is very good up to a loading of about 0.09. However, the theory predicts a discontinuity at a loading of about 0.1, whereas the simulation results still indicate smooth, albeit somewhat sharp, variations around the same point. This does indicate that the theory is capable of predicting the existence of the first-order phase transition, but the precise point where the discontinuity in the isotherm occurs is not predicted accurately by the theory.

Figure 18 presents the porosity dependence of the binary interaction parameter  $\kappa_{ab}$  for the three mixtures. As the results indicate, the interaction parameters vary essentially linearly with the porosity with slopes that are more or less the same. Moreover, the interaction parameters for the  $\text{CO}_2$ – $\text{N}_2$  and  $\text{CH}_4$ – $\text{N}_2$  mixtures are very close to each other. Observe also that, in the range of the porosities considered here,  $\kappa_{ab}$  increases as the LJ size parameter of the gas component X in the mixture X– $\text{N}_2$  decreases. Finally, at a fixed porosity, the interaction parameter  $\kappa_{ab}$  for the three mixtures varies by at most 20%. For example,

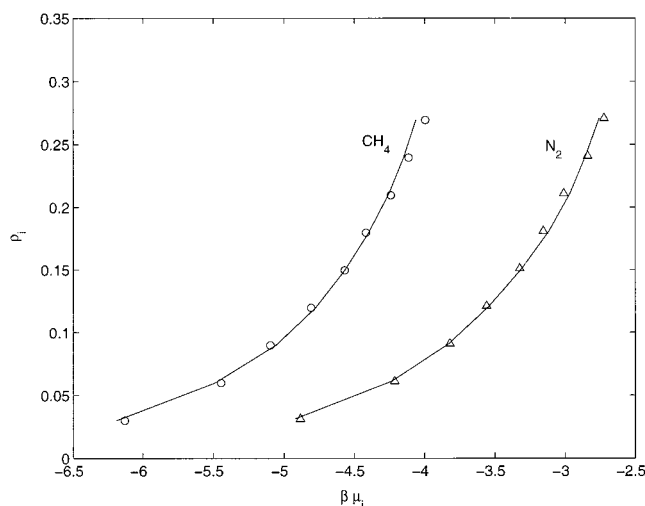


**Figure 19.** Adsorption isotherms for a binary mixture of  $\text{CH}_4$ – $\text{N}_2$  at the ideal porosity  $\varphi = 0.98$  in PCs. Symbols show the EMD simulation results, while solid curves indicate the theoretical predictions.

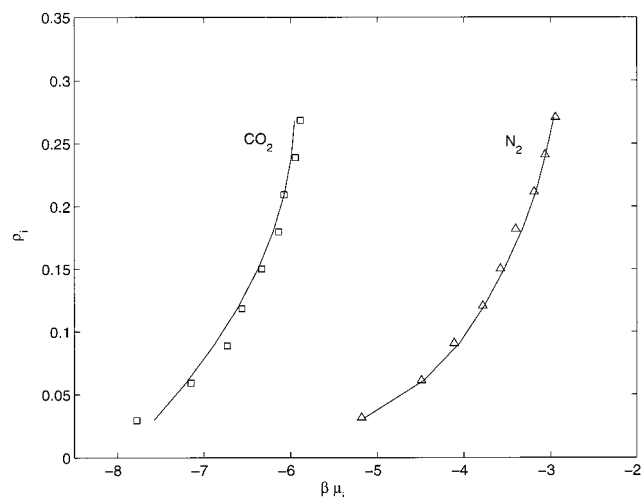


**Figure 20.** Same as in Figure 19, but for a binary mixture of  $\text{CO}_2$ – $\text{N}_2$ .

at porosity  $\varphi = 0.7$  the values of  $\kappa_{ab}$  are 0.304, 0.307, and 0.247 for  $\text{CH}_4$ – $\text{N}_2$ ,  $\text{CO}_2$ – $\text{N}_2$ , and  $\text{CF}_4$ – $\text{N}_2$ , respectively. The corresponding numbers for an ideal porosity of 0.5 are 0.175, 0.162, and 0.140. From a practical point of view, such features are very useful since they indicate that one may be able to establish simple correlations that relate the interaction parameter  $\kappa_{ab}$  to the porosity and molecular parameters of the gas components in the mixture and use the results in predicting the adsorption isotherms for a wide variety of mixtures. Work along these lines is in progress.<sup>81</sup>

**B. Adsorption in Pillared Clays.** In our previous paper<sup>37</sup> we studied in detail adsorption of single gases in PCs, where we also demonstrated that eq 21 provides excellent predictions for the EMD simulation data. Thus, in the present paper we only consider adsorption of binary gas mixtures in PCs. In the simulations that we discuss here, the total loading is fixed at 0.3 and the temperature is  $T = 303$  K.

The adsorption isotherms for  $\text{CH}_4$ – $\text{N}_2$ ,  $\text{CO}_2$ – $\text{N}_2$ , and  $\text{CF}_4$ – $\text{N}_2$  in a PC system with a porosity of 0.98 and temperature  $T = 303$  K are shown in Figures 19–21, where they are also compared with the theoretical predictions, eqs 30 and 31. The agreement between the predictions, using  $\kappa_{ab}$  as the only adjustable parameter, and the simulation results is excellent, even though we have used the relatively high loading of 0.3, which

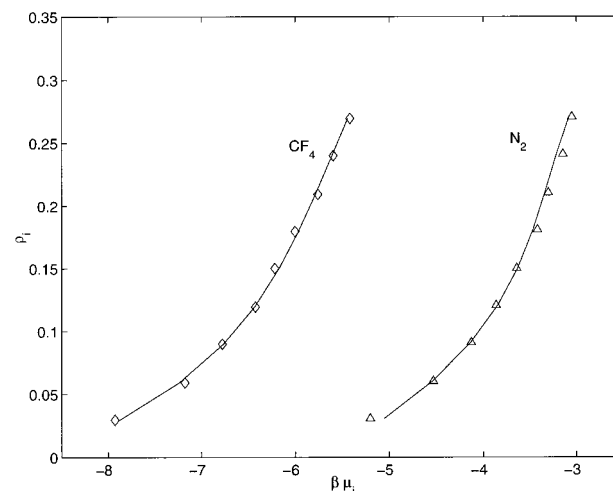


**Figure 21.** Same as in Figure 19, but for a binary mixture of  $\text{CF}_4$ – $\text{N}_2$ .

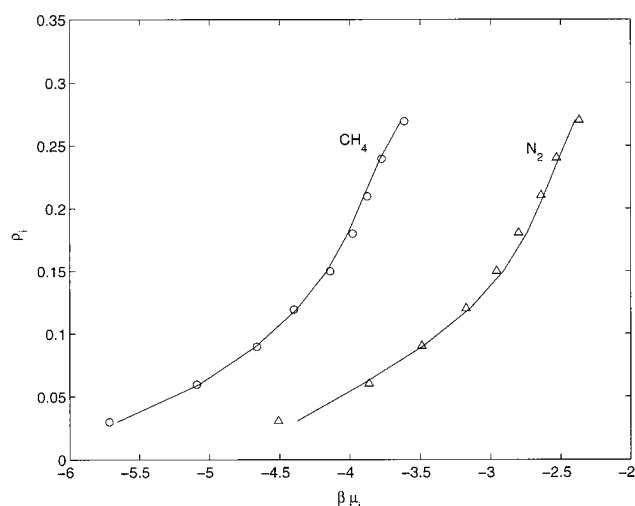


**Figure 22.** Adsorption isotherms for a binary mixture of  $\text{CH}_4$ – $\text{N}_2$  at the ideal porosity  $\varphi = 0.95$  in PCs. Symbols show the EMD simulation results, while solid curves indicate the theoretical predictions.

corresponds, for example, to pressures as high as about 90 atm for  $\text{CH}_4$  and 270 atm for  $\text{N}_2$ . Such high pressures indicate the accuracy of our statistical mechanical theory of adsorption. None of the previous theories of adsorption can predict the isotherms at such high pressures with such accuracy.

Of course, in the case of  $\text{CH}_4$ – $\text{N}_2$  mixtures, we expect our theory to be accurate, since these two gases form relatively ideal solutions. This implies that the ideal solution expressions, eqs 32 and 33, should also yield accurate results, which is indeed the case; the difference between the predictions of the two theories is very small. We note that in contrast to eqs 30 and 31, ideal solution equations require no adjustable parameters. We caution, however, that the good performance of the ideal solution equation is limited to cases where unlike adsorbate–adsorbate (i.e., a–b) interaction is Lorentz–Bertholet-like (i.e., some sort of average of the a–a and b–b interactions). If the a–b interactions were much weaker than the a–a and/or b–b interactions, then eqs 30 and 31 will perform well while eqs 32 and 33 will not. Indeed, in the case of  $\text{CO}_2$ – $\text{N}_2$  and  $\text{CF}_4$ – $\text{N}_2$  mixtures the predictions of the ideal solution expression would be very poor. If, instead, a–b interactions are much stronger than the a–a and b–b interactions, then eqs 27, 28, 32, and 33 will fail, while eqs 30 and 31 with fitted  $\kappa_{ab}$  will remain accurate.

Similar results were obtained at lower porosities. Shown in

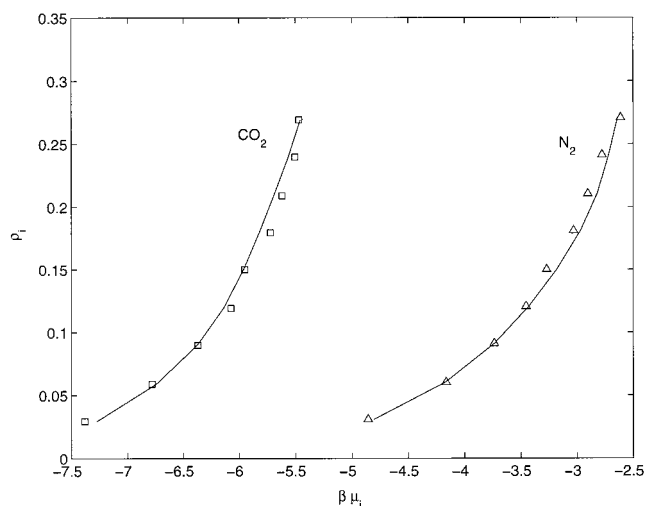


**Figure 23.** Same as in Figure 22, but for a binary mixture of  $\text{CO}_2$ – $\text{N}_2$ .

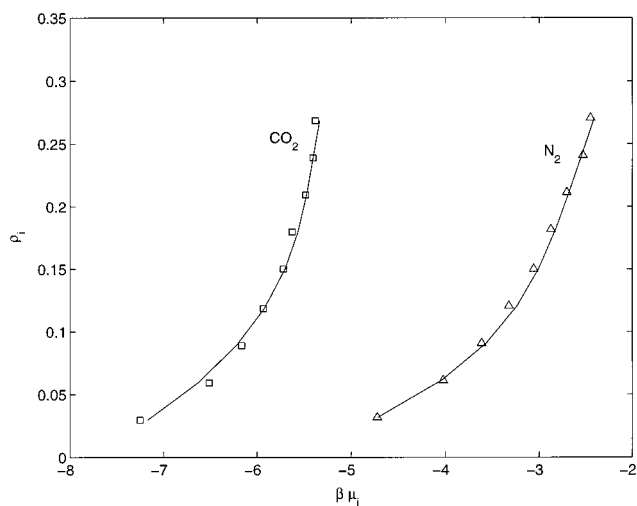


**Figure 26.** Same as in Figure 25, but for a binary mixture of  $\text{CO}_2$ – $\text{N}_2$ .

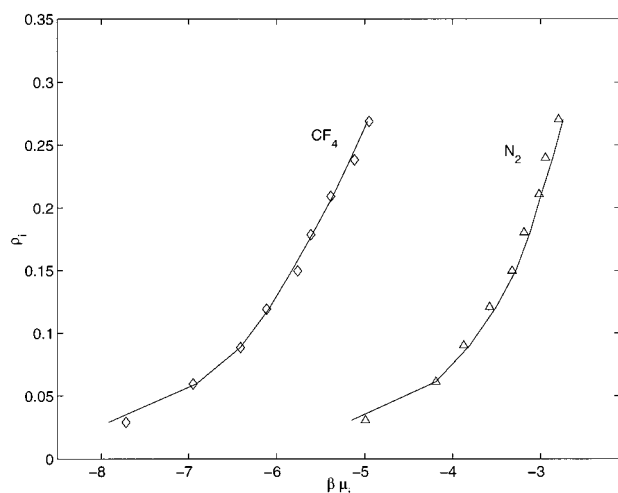


**Figure 24.** Same as in Figure 22, but for a binary mixture of  $\text{CF}_4$ – $\text{N}_2$ .

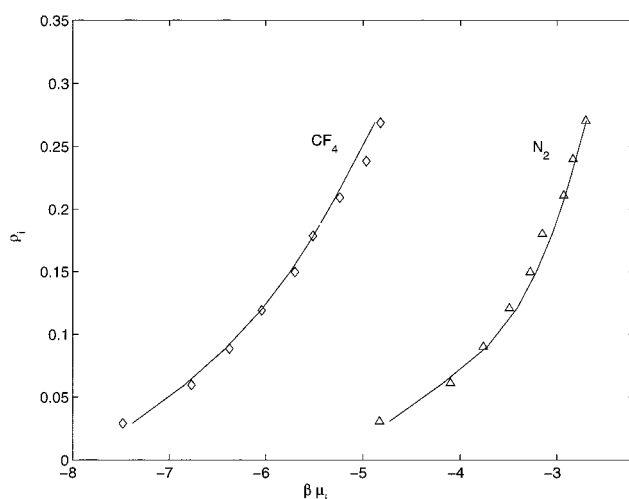


**Figure 27.** Same as in Figure 25, but for a binary mixture of  $\text{CF}_4$ – $\text{N}_2$ .

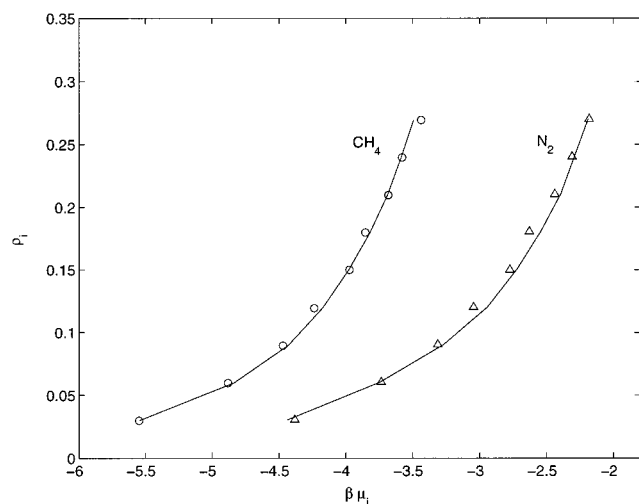


**Figure 25.** Adsorption isotherms for a binary mixture of  $\text{CH}_4$ – $\text{N}_2$  at the ideal porosity  $\varphi = 0.93$  in PCs. Symbols show the EMD simulation results, while solid curves indicate the theoretical predictions.

Figures 22–24 are the adsorption isotherms for an ideal porosity of 0.95. The agreement between the predictions and the simulation results is again very good. Finally, we show in Figures 25–27 the adsorption isotherms for the same mixtures

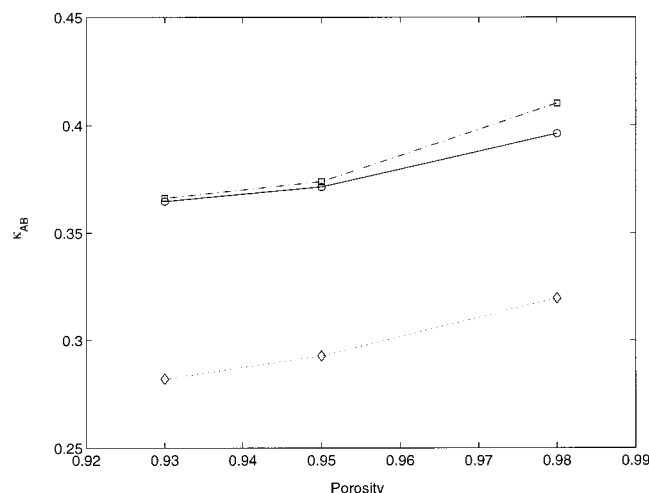
and under the same conditions as those for Figures 22–24, except that the porosity is now 0.93. The agreement between the simulation results and the predictions of the theory is again excellent. Note that, for a PC system in which the pillars consist of hard spherical particles, the percolation threshold is  $\varphi_c = 1 - \pi/18 \approx 0.83$ , much larger than that of CMSMs, modeled by the Voronoi tessellation, which is why the porosities at which we have carried out our PC simulations are much larger than those for CMSMs.

Figure 28 presents the porosity dependence of the interaction parameter  $\kappa_{ab}$  for the three mixtures in PCs. Similar to Figure 18 where we presented the porosity dependence of  $\kappa_{ab}$  for CMSMs, in the present case there is also an essentially linear dependence of the interaction parameter on the porosity. This again points to the possibility of developing simple correlations between  $\kappa_{ab}$ , the porosity, and the molecular parameters of the gases and using them in conjunction with our theory for very accurate predictions of adsorption isotherms for a wide variety of gases.

## Summary

Using EMD simulation, the adsorption equilibria of several gases and their binary mixtures in model pillared clays and carbon molecular sieve membranes were studied at room





**Figure 28.** Porosity dependence of the binary interaction parameter  $\kappa_{ab}$  for CH<sub>4</sub>-N<sub>2</sub> (circles), CO<sub>2</sub>-N<sub>2</sub> (squares), and CF<sub>4</sub>-N<sub>2</sub> (diamonds) mixtures. Dashed lines are a guide to the eye.

temperature. The results were compared with the predictions of a new statistical mechanical theory of adsorption recently developed by our group.<sup>37</sup> The theory utilizes one adjustable parameter for a one-component system. Its predictions are in excellent agreement with the simulation results. To represent the mixture adsorption data, we employed an expression based on statistical mechanical perturbation using a hypothetical system in which the cross-interaction between unlike molecular species is turned off. This is satisfactory from low to moderate loadings. At higher loadings, the correction due to the cross-interaction is then treated in an empirical manner, i.e., it is expressed by a simple regular-solution-type functional that contains an adjustable parameter and satisfies the required asymptotic behavior. Excellent agreement was found again between the predictions of the theory and the simulation results, except near a first-order phase transition point.

In future papers we will further test the ability of the theory for predicting adsorption isotherms of other binary mixtures. Of particular interest to us are temperature dependence of the adjustable parameter  $c_1$  for single gases and that of the interaction parameter  $\kappa_{ab}$  for binary mixtures, and the possibility of developing simple correlations between these parameters, the molecular parameters that represent the gas molecules, and the porosity of the microporous material. Finally, extension of our theory to adsorption of three-component gas mixtures is currently under study. The results will be reported in a future paper<sup>81</sup> in which we will also compare the predictions of our adsorption theory with experimental data.

**Acknowledgment.** This work was partially supported by the National Science Foundation. This paper is dedicated to Dr. Harvey Scher on the occasion of his 60th birthday.

## References and Notes

- (1) Patel, R. L.; Nandi, S. P.; Walker, P. L. *Fuel* **1972**, *51*, 47.
- (2) Ruthven, D. M. *Principles of Adsorption and Adsorption Processes*; Wiley: New York, 1984.
- (3) Yang, R. T. *Gas Separation by Adsorption Processes*; Butterworth: Boston, MA, 1987.
- (4) Myers, A. L.; Prausnitz, J. M. *AIChE J.* **1965**, *11*, 121.
- (5) Ruthven, D. M.; Wong, F. *Ind. Eng. Chem. Fundam.* **1985**, *24*, 27.
- (6) Sahimi, M. *Applications of Percolation Theory*; Taylor and Francis: London, 1994.
- (7) Sahimi, M. *Flow and Transport in Porous Media and Fractured Rock*; VCH: Weinheim, Germany, 1995.
- (8) Occelli, M. L.; Tindwa, R. W. *Clays Clay Miner.* **1980**, *31*, 22.
- (9) Pinnavaia, T. J. *Science* **1983**, *220*, 365.
- (10) Pinnavaia, T. J.; Landau, S. D.; Tzou, M. S.; Johnson, I. D. *J. Am. Chem. Soc.* **1985**, *107*, 7222.
- (11) Occelli, M. L.; Haru, F. S. S.; Hightower, J. W. *Appl. Catal.* **1985**, *14*, 69.
- (12) Plee, D.; Borg, F.; Gatineau, L.; Fripiat, J. J. *J. Am. Chem. Soc.* **1985**, *107*, 2362.
- (13) Tennakoon, D. T. B.; Jones, W.; Thomas, J. M.; Ballantine, J. H.; Purnell, J. H. *Solid State Ionics* **1987**, *24*, 205.
- (14) Giannelis, E. P.; Rightor, E. G.; Pinnavaia, T. J. *J. Am. Chem. Soc.* **110**, 3880.
- (15) Lee, W. Y.; Raythatha, R. H.; Tatarchuk, B. J. *J. Catal.* **1989**, *115*, 159.
- (16) Baksh, M. S.; Kikkinides, E. S.; Yang, R. T. *Ind. Eng. Chem. Res.* **1992**, *31*, 2181.
- (17) Baksh, M. S.; Yang, R. T. *Sep. Sci. Technol.* **1991**, *10*, 1377.
- (18) Baksh, M. S.; Yang, R. T. *AIChE J.* **1992**, *38*, 1357.
- (19) Yang, R. T.; Baksh, M. S. *AIChE J.* **1991**, *37*, 679.
- (20) Ohtsuka, K.; Hayashi, Y.; Suda, M. *Chem. Mater.* **1993**, *5*, 1823.
- (21) Klopogge, J. T. *Faculteit Aardwetenschappen der Rijksuniversiteit*; Utrecht, 1992.
- (22) Barrer, R. M.; MacLeod, D. M. *Trans. Faraday Soc.* **1977**, *51*, 1290.
- (23) Brindley, G. W.; Sempels, R. E. *Clay Miner.* **1977**, *12*, 229.
- (24) Yamanaka, S.; Brindley, G. W. *Clays Clay Miner.* **1978**, *26*, 21.
- (25) Lahav, H.; Shani, V.; Shabtai, J. *Clays Clay Miner.* **1978**, *26*, 107.
- (26) Vaughan, D. E. W.; Lussier, R. J. *Proceedings of the International Conference on Zeolites*; Elsevier: Amsterdam, 1980.
- (27) Grim, R. E. *Clay Mineralogy*; McGraw-Hill: New York, 1986.
- (28) Figueras, F. *Catal. Rev.-Sci. Eng.* **1988**, *30*, 457.
- (29) Cheng, L. S.; Yang, R. T. *Ind. Eng. Chem. Res.* **1995**, *34*, 2021.
- (30) Politowicz, P. A.; Kozak, J. J. *J. Phys. Chem.* **1988**, *92*, 6078.
- (31) Politowicz, P. A.; Leung, L. B. S.; Kozak, J. J. *J. Phys. Chem.* **1989**, *93*, 923.
- (32) Sahimi, M. *J. Chem. Phys.* **1990**, *92*, 5107.
- (33) Cai, Z.-X.; Mahanti, S. D.; Solin, S. A.; Pinnavaia, T. J. *Phys. Rev. B* **1990**, *42*, 6636.
- (34) Chen, B. Y.; Kim, H.; Mahanti, S. D.; Pinnavaia, T. J.; Cai, Z.-X. *J. Chem. Phys.* **1994**, *100*, 3872.
- (35) Yi, X.; Shing, K. S.; Sahimi, M. *AIChE J.* **1995**, *41*, 456.
- (36) Yi, X.; Shing, K. S.; Sahimi, M. *Chem. Eng. Sci.* **1996**, *51*, 3409.
- (37) Yi, X.; Ghassemzadeh, J.; Shing, K. S.; Sahimi, M. *J. Chem. Phys.* **1998**, *108*, 2178.
- (38) Matranga, K. R.; Stella, A.; Myers, A. L.; Glandt, E. D. *Sep. Sci. Technol.* **1992**, *27*, 1825.
- (39) Tan, Z.; Gubbins, K. E. *J. Phys. Chem.* **1992**, *96*, 845.
- (40) Cracknell, R. F.; Nicholson, D.; Quirke, N. *Mol. Phys.* **1993**, *80*, 885.
- (41) Nitta, T.; Nozawa, M.; Hishikawa, Y. *J. Chem. Eng. Jpn.* **1993**, *26*, 266.
- (42) Dunn, J.; Myers, A. L. *Chem. Eng. Sci.* **1994**, *49*, 2941.
- (43) Maddox, M. W.; Gubbins, K. E. *Langmuir* **1995**, *11*, 3988.
- (44) Maddox, M. W.; Rowlinson, J. S. *J. Chem. Soc., Faraday Trans.* **1995**, *89*, 3619.
- (45) Maddox, M. W.; Ulberg, D.; Gubbins, K. E. *Fluid Phase Equilib.* **1995**, *104*, 145.
- (46) Okayama, T.; Yoneya, J.; Nitta, T. *Fluid Phase Equilib.* **1995**, *104*, 305.
- (47) Furukuwa, S.-I.; Shigeta, T.; Nitta, T. *J. Chem. Eng. Jpn.* **1996**, *29*, 725.
- (48) Segarra, E. I.; Glandt, E. D. *Chem. Eng. Sci.* **1994**, *49*, 2953.
- (49) Koresh, J. E.; Sofer, A. *Sep. Sci. Technol.* **1983**, *18*, 723.
- (50) Bourgerette, C.; Oberlin, A.; Inagaki, M. *J. Mater. Res.* **1992**, *7*, 1158.
- (51) Hishiyama, Y.; Yoshida, A.; Kaburagi, Y.; Inagaki, M. *Carbon* **1992**, *30*, 333.
- (52) Hatori, H.; Yamada, Y.; Shiraishi, M. *Carbon* **1993**, *30*, 763; **1993**, *31*, 1307.
- (53) Mariawala, R. K.; Foley, H. C. *Ind. Eng. Chem. Res.* **1994**, *33*, 607.
- (54) Emmerich, F. G. *Carbon* **1995**, *33*, 1709.
- (55) Jones, C. W.; Koros, W. J. *Carbon* **1994**, *32*, 1419, 1427.
- (56) Jones, C. W.; Koros, W. J. *Ind. Eng. Chem. Res.* **1995**, *34*, 158, 164; **1996**, *35*, 2999.
- (57) Sedigh, M. G.; Onstot, W. J.; Xu, L.; Peng, W. L.; Tsotsis, T. T.; Sahimi, M. *J. Phys. Chem. A* **1998**, *102*, 8580.
- (58) Sedigh, M. G.; Xu, L.; Tsotsis, T. T.; Sahimi, M. *Ind. Eng. Chem. Res.* **1999**, *38*, 3367.
- (59) Xu, L.; Sedigh, M. G.; Sahimi, M.; Tsotsis, T. T. *Phys. Rev. Lett.* **1998**, *80*, 3511.
- (60) Xu, L.; Tsotsis, T. T.; Sahimi, M. *J. Chem. Phys.* **1999**, *111*, 3252.
- (61) Xu, L.; Sedigh, M. G.; Tsotsis, T. T.; Sahimi, M. *J. Chem. Phys.* **2000**, *112*, 910.

- (62) June, R. L.; Bell, A. T.; Theodorou, D. N. *J. Phys. Chem.* **1990**, *94*, 1508; **1990**, *94*, 8232; **1991**, *95*, 8866.
- (63) Maggin, E. J.; Bell, A. T.; Theodorou, D. N. *J. Phys. Chem.* **1993**, *97*, 4173.
- (64) Snurr, R. Q.; Bell, A. T.; Theodorou, D. N. *J. Phys. Chem.* **1993**, *97*, 13742.
- (65) Steele, W. A. *Surf. Sci.* **1973**, *36*, 317.
- (66) Gear, C. W. *Numerical Initial Value Problems in Ordinary Differential Equations*; Prentice-Hall: Englewood Cliffs, NJ, 1971.
- (67) Haile, J. M. *Molecular Dynamics Simulations*; Wiley: New York, 1990.
- (68) Widom, B. *J. Chem. Phys.* **1963**, *39*, 2808.
- (69) Widom, B. *J. Phys. Chem.* **1963**, *86*, 869.
- (70) Shing, K. S.; Gubbins, K. E. *Mol. Phys.* **1981**, *43*, 717; **1982**, *46*, 1109.
- (71) Deitrick, G. L.; Scriven, L. E.; Davis, H. T. *J. Chem. Phys.* **1989**, *90*, 2370.
- (72) Schultz, M. H. *Spline Analysis*; Prentice-Hall: Englewood Cliffs, NJ, 1973.
- (73) Kahaner, D.; Moler, C.; Nash, S. *Numerical Methods and Software*; Prentice-Hall: Englewood Cliffs, NJ, 1989.
- (74) Jaroniec, M. J.; Choma, J.; Lu, X. *Chem. Eng. Sci.* **1981**, *36*, 3299.
- (75) Horvath, G.; Kawazoe, K. *J. Chem. Eng. Jpn.* **1983**, *16*, 470.
- (76) Moore, D. M.; Reynolds, R. C. *X-Ray Diffraction and the Identification and Analysis of Clay Minerals*; Oxford University Press: London, 1989.
- (77) Rowlinson, J. S. *Proc. R. Soc. London, Ser. A* **1985**, *402*, 67.
- (78) Rowlinson, J. S. *J. Chem. Soc., Faraday Trans.* **1986**, *82*, 1809.
- (79) Woods, G. B.; Panagiotopoulos, A. Z.; Rowlinson, J. S. *Mol. Phys.* **1988**, *63*, 49.
- (80) Johnson, J. K.; Zollweg, J. A.; Gubbins, K. E. *Mol. Phys.* **1993**, *78*, 591.
- (81) Ghassemzadeh, J.; Sahimi, M. *Chem. Eng. Sci.*, in press.